Title: Multicentennial AMOC Variability Shaped the Hydroclimatic Stage for the Tubo Empire

Authors: Fengli An[1], Haijun Yang[1]*, Qiong Zhang[2], Zhenqian Wang[2], Likun Han[1], Juzhi Hou[3], Hao Li[4]

Affiliations:

[1]Department of Atmospheric and Oceanic Sciences and Key Laboratory of Polar Atmosphere-ocean-ice System for Weather and Climate of Ministry of Education, Fudan University, Shanghai, 200438, China.

[2]Department of Physical Geography and Bolin Centre for Climate Research, Stockholm University, Stockholm, 10691, Sweden.

[3]Group of Alpine Paleoecology and Human Adaptation, State Key Laboratory of Tibetan Plateau Earth System, Resources and Environment, Institute of Tibetan Plateau Research, Chinese Academy of Sciences, Beijing 100101, China.

[4]State Key Laboratory of Lithospheric and Environmental Coevolution, Institute of Geology and Geophysics, Chinese Academy of Sciences, Beijing 100101, China.

*Corresponding author. Email: yanghj@fudan.edu.cn

Abstract: Long-term climate variability is increasingly recognized as a driver of societal change. Here we combine paleoclimate records, historical documents, and a transient simulation with the EC-Earth3 model to assess how Atlantic Meridional Overturning Circulation (AMOC) variability shaped Tibetan Plateau hydroclimate during the rise and fall of the Tubo Empire (~600–900 CE). A strong AMOC shifted the Intertropical Convergence Zone northward, intensified the Indian summer monsoon, and produced ~10% wetter summers over the southwestern Plateau, coinciding with Tubo expansion. A weak AMOC drove the opposite pattern, aligning with the empire's ninth-century decline. While political and religious factors undoubtedly contributed, these results highlight the large-scale long-term climate mode as a critical backdrop for societal trajectories and a warning for future water security in Asia.

Main Text:

The Tubo Empire (Fig. 1), which thrived from the early 7th to the mid-9th century CE, was the first historically unified regime across the Qinghai–Tibetan Plateau (TP) (*1-3*). During this period, the region experienced major political consolidation, population growth, and cultural development, leaving a lasting historical legacy among China's multiethnic civilizations (*3*). At its zenith, the Tubo Empire stood as a major regional power alongside contemporaneous states such as the Tang Dynasty, the Abbasid Caliphate, and the Harsha Empire, reflecting its broad geopolitical influence across Central and South Asia (*2-6*).

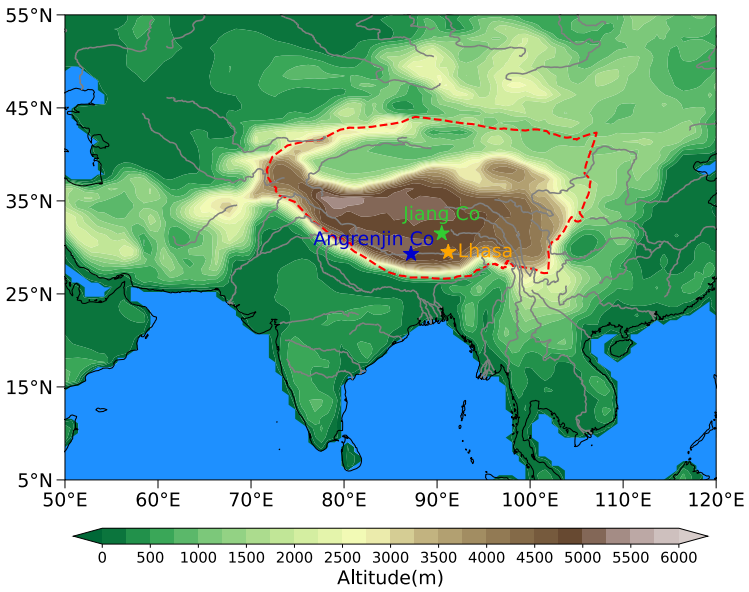

Fig. 1. Topography of the Tibetan Plateau and surrounding regions. The dashed red curve outlines the approximate extent of the Tubo Empire at its peak around 800 CE (*7*). The orange star marks the location of Lhasa, the imperial capital. Blue and green stars indicate the locations of Lake Angrenjin Co and Jiang Co, respectively.

Despite its formidable strength and cultural achievements, the Tubo Empire entered a period of rapid decline in the late 9th century (*2, 3, 8*). Its collapse was followed by a prolonged era of political fragmentation across the Plateau, with no comparable unification until the modern period. Historians and archaeologists have attributed the empire's fall to a variety of factors, including political instability, succession disputes, religious conflicts between Buddhism and the indigenous Bon religion, popular uprisings, natural disasters, and disease outbreaks (*3-6*, *9*). Yet the limited availability of contemporaneous historical records and archaeological evidence has left the primary cause unresolved.

Among these contributing factors, the fragile natural environment of the TP warrants particular attention. Often referred to as the "Third Pole" and the "Asian Water Tower," the Plateau is highly sensitive to changes in global temperature, the Asian monsoon, and the midlatitude westerlies (*10-16*). These climatic drivers have a profound impact on regional

agriculture, water availability, and human livelihoods, making environmental stability a cornerstone of societal resilience in the region (*17, 18*). In this context, it is both imperative and timely to investigate whether long-term climate variability may have contributed to the rise and fall of the Tubo civilization.

Paleoclimate reconstructions provide growing evidence for such a link. A high-resolution pollen record from Angrenjin Co in the southern TP revealed ~500-year and ~210-year wet–dry climatic cycles, superimposed on a longer-term drying trend attributed to declining summer insolation (*17*). These cycles were supposed to be linked to sea surface temperature (SST) variability in the tropical Pacific and Indian Oceans, as well as shifts in the midlatitude westerlies. The superposition of 500-year and 210-year modes may have shaped the Tubo trajectory: wetter phases (~600–650 and ~750–800 CE) coincided with expansion, whereas a prolonged dry episode (~850–900 CE) overlapped with decline (*17*). Similarly, records from Jiang Co suggested that the Tubo Empire's peak corresponded to a ~200-year warm–wet interval, while its collapse occurred during a colder, drier phase (*18*). These findings suggest that hydroclimatic changes influenced the empire's agricultural base and societal stability.

Yet proxy records alone cannot fully resolve the physical mechanisms. Were these fluctuations driven primarily by external forcings, such as solar variability, or by internal climate dynamics? Answering this question is critical for understanding both the environmental history of the Tubo Empire and the broader role of low-frequency variability in shaping human societies. Multicentennial variability is a pervasive feature of Holocene archives, appearing in ice cores, speleothems, lacustrine sediments, and marine records worldwide (*19*). Coupled climate models likewise generate internally sustained oscillations of the Atlantic Meridional Overturning Circulation (AMOC) on multicentennial timescales, arising from advective–salinity feedbacks and atmosphere–ocean interactions (*20*, *21*). The convergence of proxy evidence and model dynamics underscores the robustness of such long-period AMOC variability and provides a compelling motivation to examine its influence on ancient Asian hydroclimates.

By combining high-resolution proxy data (*17*, *18*), historical records (*22*), and a historical transient simulation with the EC-Earth3 coupled model (*23*), our analysis identifies a robust relationship between multicentennial AMOC oscillations and hydroclimatic variability over the TP, suggesting a link of the Tubo Empire's trajectory to multicentennial AMOC variability. By situating the TP within a broader ocean–atmosphere teleconnection framework, we show how large-scale climate mode can provide an environmental backdrop for societal change.

Coherence between AMOC variability and hydroclimate over the TP

The leading low-frequency components (LFC1) of summer precipitation and surface air temperature (SAT) over the Tubo region track multicentennial AMOC variability with striking fidelity. These modes also show coherence with proxy records and the historical

timeline of 600–900 CE. Figures 2A–C present the LFC1 time series for precipitation, SAT across the broader South and East Asian monsoon domain (50°E–120°E, 5°–55°N), and the AMOC, respectively, derived from the EC-Earth3 transient simulation (*23*). All exhibit pronounced multicentennial variability with a dominant periodicity of ~160 years (fig. S1). Periods of stronger AMOC align with warmer and wetter conditions, while weaker AMOC corresponds to cooler and drier states. This pattern is particularly evident during the Tubo Empire (~600–900 CE, light-yellow shading).

The modeled signals agree with high-resolution proxy archives. The $\delta^{18}O$ record from Jiang Co (Fig. 2E), a hydroclimate-sensitive indicator, shifts in phase with both precipitation and AMOC during the Tubo period. An alkenone-based temperature reconstruction from the same site records a transition from relatively warm to cooler conditions. The Ti concentration record (Fig. 2F), reflecting catchment erosion and runoff, suggests reduced monsoonal input during the late empire. Similarly, the pollen-based precipitation reconstruction from Angrenjin Co (Fig. 2G) documents a wet-to-dry transition, while central-eastern China SAT reconstructed from historical documents (Fig. 2H) shows a parallel change. Collectively, these datasets point to a coherent warm–wet regime during the Tubo Empire's flourishing stage, followed by a cool–dry regime during its decline.

This alignment between modeled and proxy-based hydroclimatic changes and the historical trajectory of the Tubo Empire suggests a potential role of multicentennial AMOC variability in shaping the Plateau's environmental conditions. The relationship is particularly evident between 650 and 750 CE, when AMOC reached its strongest amplitude, coinciding with a sustained warm–wet phase. Comparable but lower-amplitude fluctuations appear during other periods (Fig. 2, gray shading), reinforcing the persistence of this mechanism.

The physical linkage is already implied in Fig. 2. Both the Indian summer monsoon rainfall (ISMR; Fig. 2D, green) and the Intertropical Convergence Zone (ITCZ) latitude (Fig. 2D, orange) covary strongly with AMOC LFC1 (Fig. 2C), with correlations of ~0.90 and ~0.80, respectively. A stronger AMOC is associated with a northward-shifted ITCZ and intensified ISMR, facilitating enhanced moisture transport into the southern and southwestern Plateau. Conversely, weaker AMOC coincides with a southward ITCZ, reduced ISMR, and drier conditions.

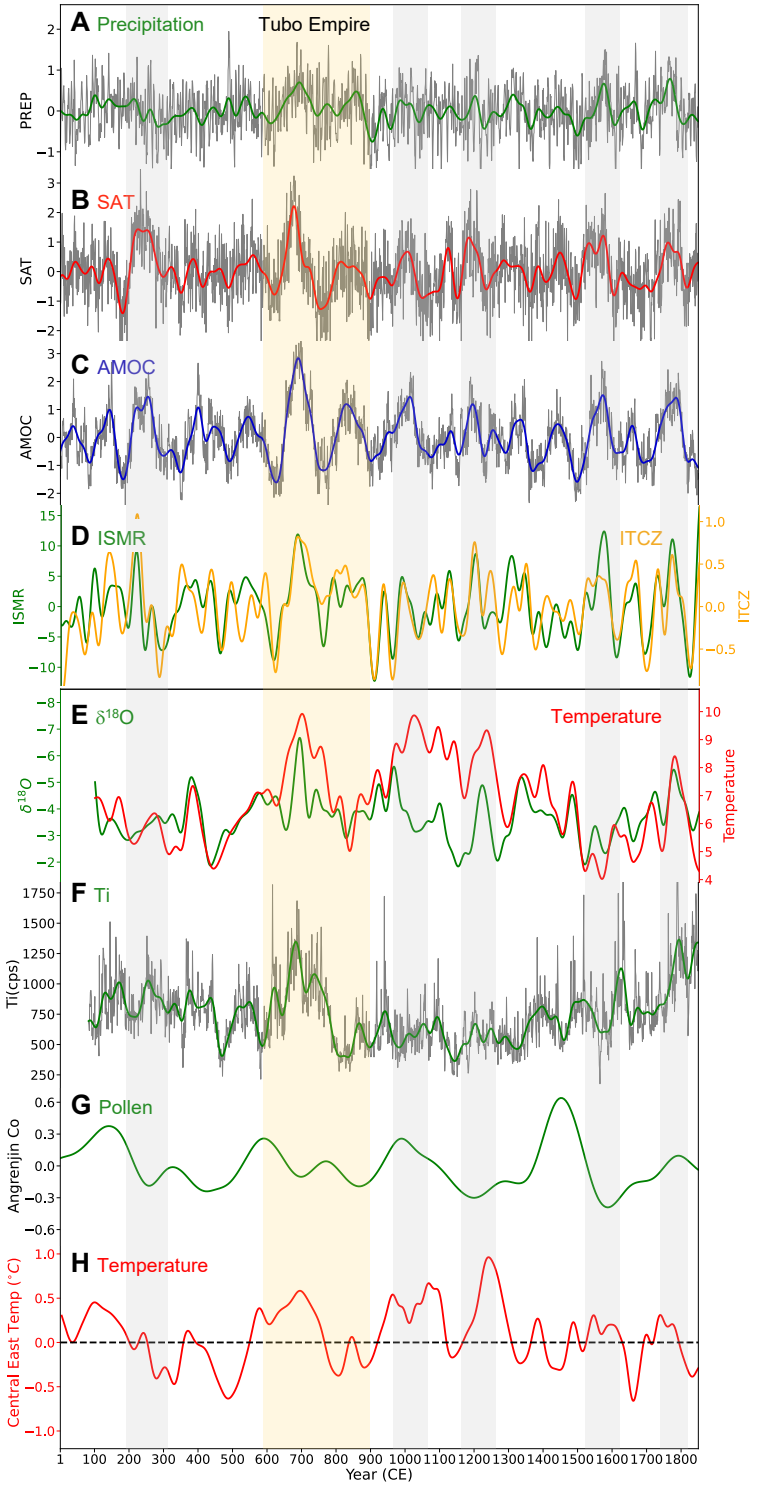

Fig. 2. Time series of model output (A-D), proxy evidence (E-G) and historical record (H). (**A**, **B**) Normalized first low-frequency component (LFC1) of summer precipitation and surface air temperature (SAT) over the Tubo region. (**C**) LFC1 of the AMOC. (**D**) Indexes for Indian summer monsoon rainfall (ISMR; green; mm month^{-1}) and latitudinal position of the Intertropical Convergence Zone (ITCZ; orange; degree). For ITCZ, positive (negative) value denotes northward (southward) displacement in relative to its climatological mean position. (**E**) Jiang Co sediment: $\delta^{18}O$

record (green) and temperature reconstruction based on the alkenone unsaturation index U_{37}^{K} (red, °C) (*18*). (**F**) Titanium (Ti) concentration from XRF scanning of the same core. Panels e-f are from Hou et al. (2023). (**G**) Pollen-based precipitation reconstruction from Angrenjin Co (*17*). (**H**) SAT anomaly (°C) for central-eastern China derived from Chinese historical documents (*22*). Thick curves in panels **A-H** are low-pass-filtered. See (*23*) for data processing procedures. Light-yellow band denotes the Tubo Empire period (~600–900 CE). The proxy data and the historical record are all linear interpolated to have resolution of one-year.

This chain of connections—variation of AMOC strength shifts the ITCZ latitude, which affects ISMR intensity and TP precipitation—provides a physically consistent mechanism for AMOC-driven hydroclimate modulation. The critical link lies in the ITCZ's sensitivity to interhemispheric energy balance. A large body of paleoclimate evidence (*24-27*), theoretical work (*28, 29*), and model simulations (*30-36*) demonstrates that a stronger AMOC drives northward ITCZ displacement, while a weaker AMOC pushes it southward. These latitudinal shifts in the tropical rainfall belt directly modulate monsoon strength and moisture advection into the Plateau. The coupled ocean–atmosphere mode identified in our simulation aligns so closely with the Tubo Empire's rise and fall, suggesting that large-scale low-frequency variability may have set the environmental stage for societal resilience and vulnerability on the TP.

Manifestation of AMOC in the hydroclimate change over the TP

To assess how multicentennial AMOC variability manifests spatially, we compare the leading low-frequency patterns (LFP1s) of modeled summer precipitation and SAT (*23*) with regression fields obtained by projecting global fields onto the AMOC LFC1 index in Fig. 3. The precipitation LFP1 (Fig. 3A) shows a coherent wet anomaly extending from the southwestern TP across the Indian subcontinent to the Bay of Bengal, with amplitudes of ~10% of the summer climatological mean (fig. S2). The AMOC-related precipitation regression (Fig. 3B) reproduces both structure and magnitude, with a pattern correlation above 0.80 ($p < 0.01$). A similar correspondence appears for SAT: the LFP1 pattern (Fig. 3C) reveals warming across most of the region, flanked by cooling over the Indian subcontinent, while the AMOC regression (Fig. 3D) yields a nearly identical dipole (pattern correlation ~0.80). These matches demonstrate that multicentennial AMOC variability is the principal driver of low-frequency hydroclimatic anomalies over the TP.

To investigate the physical pathway connecting AMOC variability to hydroclimatic conditions over the TP, we first examine the LFP1 of AMOC itself. The AMOC LFP1closely resembles the climatological structure of the AMOC (fig. S3), suggesting the LFC1 mode captures the internal variability of the background AMOC — not an alternative mode of overturning, representing a simple intensification/weakening of the background AMOC. Since the climatological AMOC structure is responsible for northward heat transport,

especially into the North Atlantic, fluctuations in this structure's strength imply modulations in interhemispheric energy balance. This links directly to the ITCZ's shift (*28, 33*).

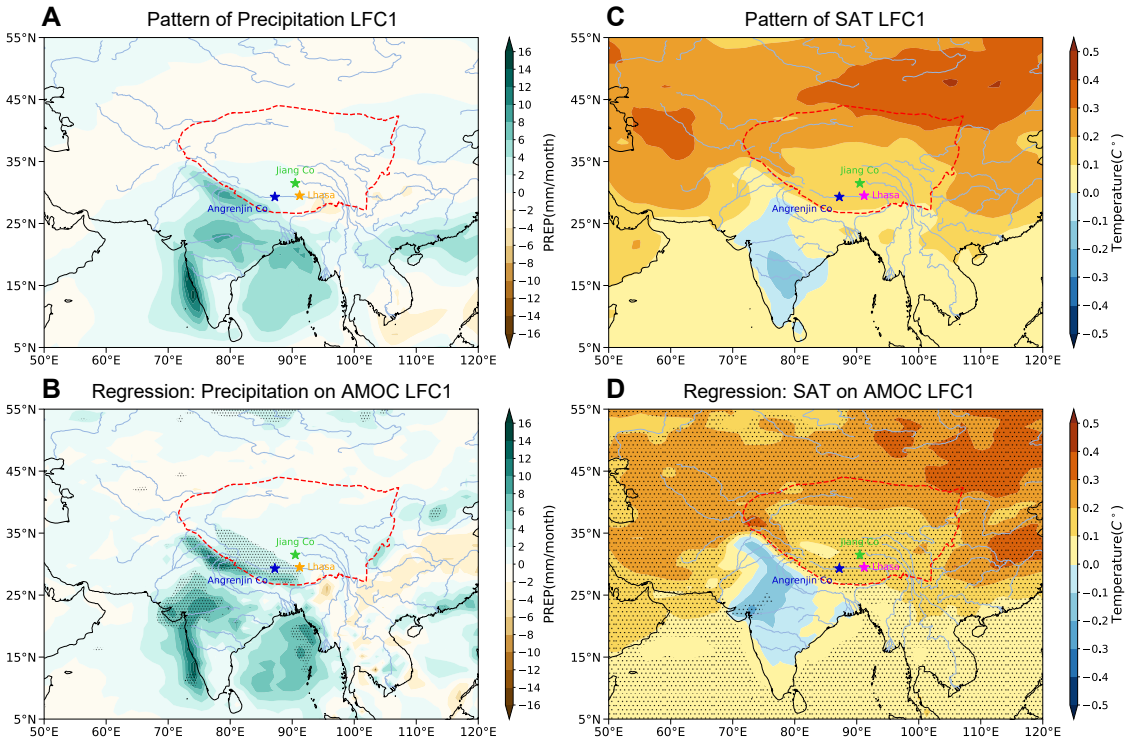

Fig. 3. Spatial expression of AMOC-related low-frequency variability in EC-Earth3. (**A**) LFC1 pattern of summer precipitation (mm month^{-1}). (**B**) Regression of summer precipitation onto the low-pass-filtered AMOC LFC1 index, shown over the same domain as (**A**); stippling denotes 99% significance. (**C, D**) Same as (**A, B**), but for summer SAT (°C). Patterns in (**A**, **C**) correspond to 1 standard deviation of the precipitation and SAT indexes in Fig. 2, A and B, respectively. Regressions in (**B**, **D**) correspond to 1 standard deviation of the AMOC LFC1 index in Fig. 2C.

The AMOC LFC1 is associated with a basin-wide SST anomaly in the North Atlantic (Fig. 4A), nearly identical to the SST pattern obtained by regressing global SST onto the TP precipitation LFC1 (fig. S4B). Leading SAT modes linked to AMOC and TP precipitation mirror these SST anomalies (fig. S4, C-D), suggesting SAT changes primarily reflect SST forcing. Higher temperatures would have aided crop farming by facilitating snowmelt and raising the maximum planting altitude of highland barley, the Tubo Empire's staple crop (*37*). Thus, the North Atlantic SST anomaly acts as a key intermediary transmitting AMOC variability to TP hydroclimate.

To identify the atmospheric bridge, we regressed 500-hPa geopotential height onto the low-pass-filtered AMOC LFC1 (Fig. 4B). The result reveals a planetary stationary Rossby-wave train emanating from the North Atlantic and propagating eastward across Eurasia. Three corridors of influence are discernible: (1) a subtropical westerly pathway along 30°–40°N, linking the Atlantic to western China via the Asian jet; (2) a North Pacific pathway affecting

northern China; and (3) a southwestern monsoon pathway, whereby the Indian summer monsoon can influence the southern Plateau.

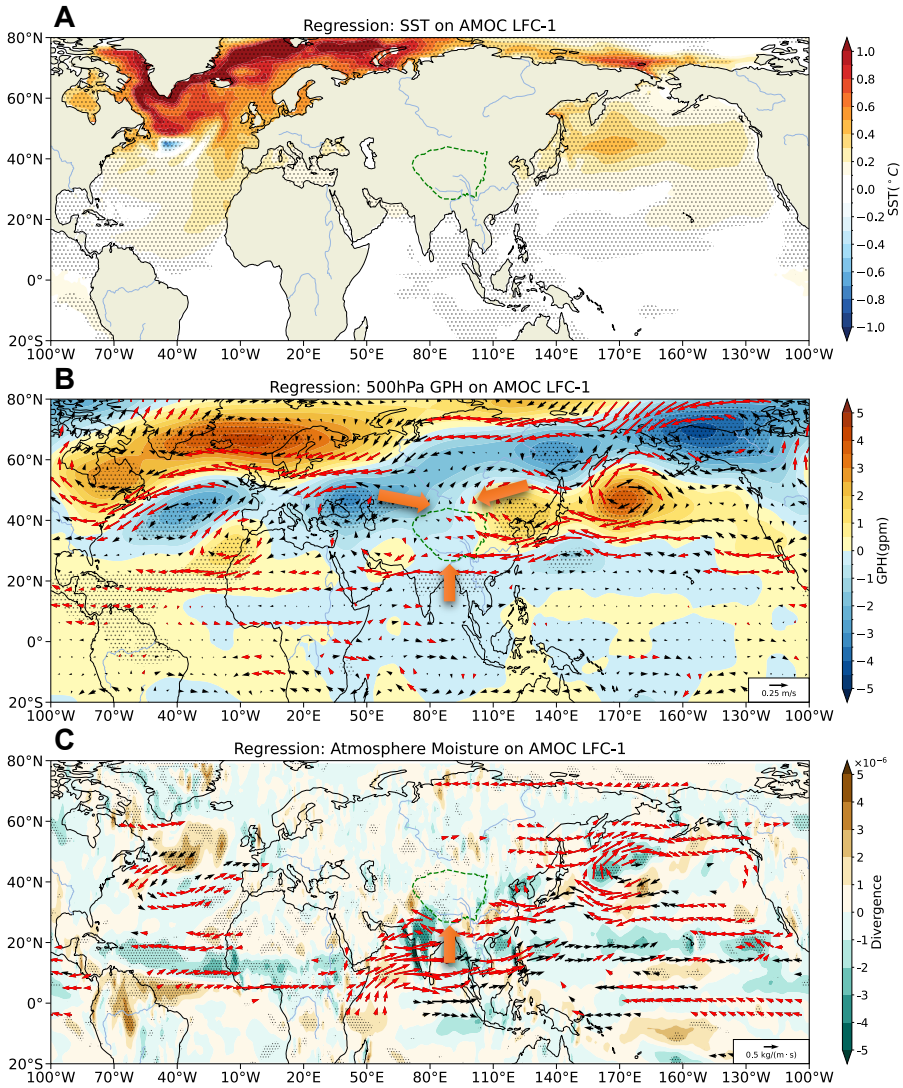

Fig. 4. North Atlantic–Eurasian teleconnection associated with the AMOC LFC1 mode. (**A**) Regression of global SST (°C) onto the AMOC LFC1 index. (**B**) Regression of 500-hPa geopotential height (GPH; m, shading) and wind anomalies (vectors; reference arrow: 0.25 m s^{-1}) onto the same index. (**C**) Regression of vertically integrated moisture-flux divergence (shading, 10^{-6} kg m^{-2} s^{-1}) and moisture-flux anomalies (vectors; reference arrow: 0.5 kg m^{-1} s^{-1}). Green (brown) shading denotes convergence (divergence). Stippling marks 99% significance. In (**B**, **C**), red vectors mark 90% significance, and thick orange arrows denotes pathways that potentially affect the Tubo region. All regressions correspond to 1 standard deviation of the AMOC LFC1 index in Fig. 2C.

However, the anomalous moisture flux points to a single dominant conduit. Regression of vertically integrated moisture transport and flux convergence onto AMOC LFC1 (Fig. 4C) shows that during strong-AMOC phases, southwesterly anomalies extend northeastward from

the tropical Indian Ocean and Bay of Bengal into the southwestern TP. This pattern is consistent with a northward-displaced ITCZ. In contrast, the midlatitude Rossby-wave branches identified in Fig. 4B contribute little net moisture to the Plateau. Thus, AMOC variability influences the summer TP hydroclimate primarily via the monsoon–ITCZ pathway, not extratropical stationary waves.

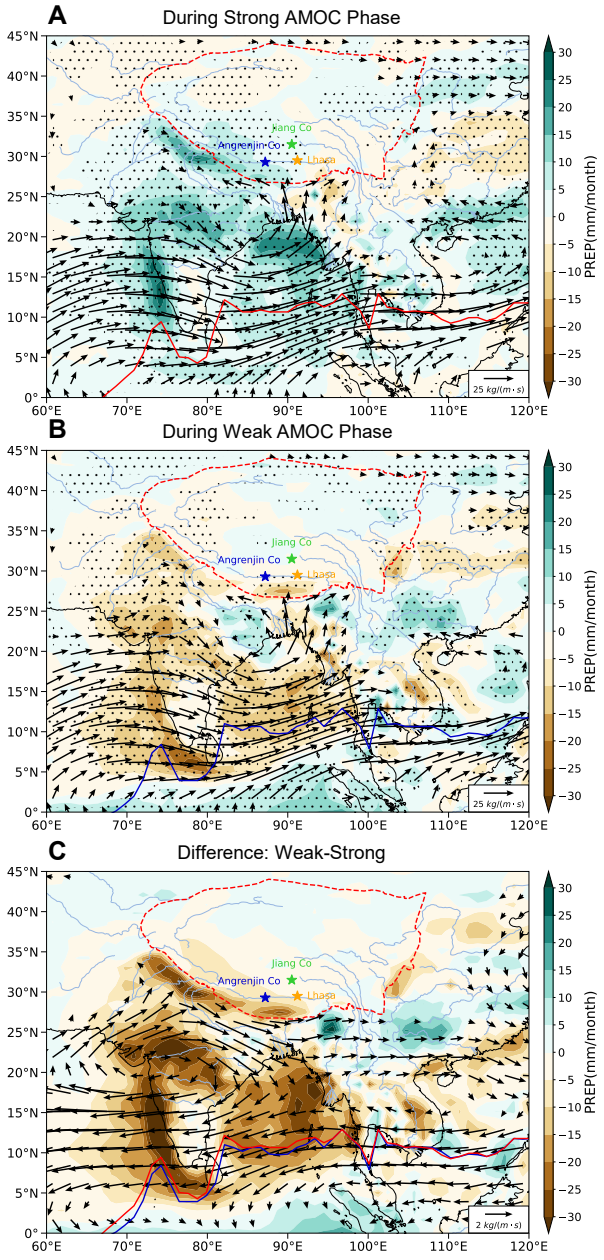

Fig. 5. Composite analysis of summer hydroclimate anomalies for contrasting two AMOC states. (**A**) Strong AMOC phases. (**B**) Weak AMOC phases. (**C**) Difference (weak – strong). Colors indicate precipitation anomalies (mm month^{-1}); arrows show vertically integrated moisture flux anomalies (kg m^{-1} s^{-1}). Climatological mean precipitation during 600-900 CE is removed. Solid red (blue) curve denotes the ITCZ position during strong (weak) AMOC phase. Stippling in (**A**, **B**) marks significance at the 99% level.

To visualize the net effect, we constructed composites of summer precipitation and vertically integrated moisture-flux anomalies for strong, weak, and contrasting AMOC phases (Fig. 5). During strong-AMOC phases (Fig. 5A), a northeastward moisture corridor develops from the Bay of Bengal, delivering widespread precipitation surpluses across the southwestern TP and the Yarlung Tsangpo headwaters under orographic uplift. This is consistent with a northward ITCZ (Fig. 5A, Red curve). During weak-AMOC phases (Fig. 5B), the corridor weakens, and precipitation deficits spread across the TP, Indian subcontinent, and Bay of Bengal. The difference field (Fig. 5C, weak minus strong) highlights a ~30 mm month^{-1} swing in summer rainfall and a reversal of moisture flux relative to strong-AMOC conditions. The drying is accompanied by lower SAT across the Tubo heartland and warmer SAT over the Indian subcontinent (fig. S5).

Our results extend earlier proxy-based suggestions that TP hydroclimate oscillates on ~200- to 500-yr scales (*17, 18*) by providing a physically consistent ocean–atmosphere pathway. The coherence between AMOC variability and Tibetan Plateau hydroclimate is consistent with the broader fingerprint of multicentennial variability evident in Holocene proxy records and in coupled climate models. That convergence strengthens confidence that the Tubo case reflects not an isolated coincidence, but the expression of a pervasive mode of low-frequency climate variability with societal relevance.

These findings reinforce the view that low-frequency oceanic modes can exert regionally selective hydroclimate control, influencing societal trajectories even without large external forcing. Similar diagnostics could be applied to contemporaneous polities such as the Tang Dynasty or the Abbasid Caliphate. In addition, given increasing evidence for a 21st-century AMOC weakening (*38–41*), our results suggest that a persistent downturn could favor southward ITCZ displacement, monsoon weakening, and drying of the TP—potentially stressing water resources for more than 100 million downstream residents.

References and Notes

1. X. Liu, *Old Tang Dynasty History*. vol. 196 (Tubo Volume) (Zhonghua Book Company, Press (In Chinese), 1975).
2. B. Xian, *A Brief History of Tibetans in Qinghai (In Chinese)*. (Qinghai People's Publishing House, 2014).
3. Y. Zhang, G. Lin, *A General History of Tibet*. (China Tibetology Press, Beijing (In Chinese), 2016).
4. Y. Zhu, *Historical Military Geography of Tubo Dynasty (In Chinese)*. (China Social Sciences Press, 2017).
5. Y. Zhang, *The Tubo Silk Road (In Chinese)*. (Jiangsu People's Publishing House, 2017).

6. Y. Zhang, *Study on Tubo History and Northwest Ethnic History in Tang Dynasty (In Chinese)*. (Jiangsu People's Publishing House, 2021).
7. Q. Tan, The Historical Atlas of China (in Chinese). (China Cartographic Publishing House, 1996).
8. X. Wang, *History of Political Relations between the Tang, Tubo and Arab Empires (In Chinese)*. (SDX Joint Publishing Company, 2022).
9. R. Xu, The collapse of Tubo regime and its population flow in the perspective of climate change (in Chinese). *China Tibetology* (2024).
10. T. Yao *et al.*, A review of climatic controls on δ18O in precipitation over the Tibetan Plateau: Observations and simulations. *Reviews of Geophysics* **51**, 525–548 (2013).
11. Y. Ma, M. Lu, H. Chen, M. Pan, Y. Hong, Atmospheric moisture transport versus precipitation across the Tibetan Plateau: A mini-review and current challenges. *Atmospheric Research* **209**, 50–58 (2018).
12. X. Liu, X. Zhang, Y. Lin, L. Jin, F. Chen, Strengthened Indian summer monsoon brought more rainfall to the western Tibetan Plateau during the early Holocene. *Science Bulletin* **64**, 1482-1485 (2019).
13. Y. Song *et al.*, Agricultural Adaptation to Global Warming in the Tibetan Plateau. *IJERPH* **16**, 3686 (2019).
14. F. Chen *et al.*, Climate change, vegetation history, and landscape responses on the Tibetan Plateau during the Holocene: A comprehensive review. *Quaternary Science Reviews* **243**, 106444 (2020).
15. T. Yao, X. Liu, N. Wang, Y. Shi, Amplitude of climatic changes in Qinghai-Tibetan Plateau. *Chinese Sci. Bull.* **45**, 1236–1243 (2000).
16. A. Cui *et al.*, Tibetan Plateau Precipitation Modulated by the Periodically Coupled Westerlies and Asian Monsoon. *Geophysical Research Letters* **48**, e2020GL091543 (2021).
17. H. Li *et al.*, Multicentennial climate cycles and their impact on the Tubo Dynasty in the southern Tibetan Plateau. *Palaeogeography, Palaeoclimatology, Palaeoecology* **578**, 110584 (2021).
18. J. Hou *et al.*, Climate change fostered rise and fall of the Tibetan Empire during 600–800 AD. *Science Bulletin* **68**, 1187–1194 (2023).
19. T. G. Askjær *et al.*, Multi-centennial Holocene climate variability in proxy records and transient model simulations. *Quaternary Science Reviews* **296**, 107801 (2022).
20. N. Cao *et al.*, The role of internal feedbacks in sustaining multi-centennial variability of the Atlantic Meridional Overturning Circulation revealed by EC-Earth3-LR simulations. *Earth and Planetary Science Letters* **621**, 118372 (2023).

21. K. Yang, H. Yang, Y. Li, Q. Zhang, North Atlantic Ocean–originated multicentennial oscillation of the AMOC: A coupled model study. *Journal of Climate* **37,** 2789-2807 (2024).

22. Q. Ge, Z. Hao, J. Zheng, X. Shao, Temperature changes over the past 2000 yr in China and comparison with the Northern Hemisphere. *Clim. Past* **9**, 1153–1160 (2013).

23. Materials and methods are available as supplementary materials.

24. T. Schneider, Migrations and dynamics of the intertropical convergence zone. *Nature* **513**, 45–53 (2014).

25. Y. T. Hong *et al.*, Correlation between Indian Ocean summer monsoon and North Atlantic climate during the Holocene. *Earth and Planetary Science Letters* **215**, 317–318 (2003).

26. H. Xu, Y. Song, Y. Goldsmith, Y. Lang, Meridional ITCZ shifts modulate tropical/subtropical Asian monsoon rainfall. *Science Bulletin* **64**, 1737–1739 (2019).

27. J. Zhao *et al.*, Orchestrated decline of Asian summer monsoon and Atlantic meridional overturning circulation in global warming period. *The Innovation Geoscience* **1**, 1–9 (2023).

28. A. Donohoe, J. Marshall, D. Ferreira, D. Mcgee, The Relationship between ITCZ Location and Cross-Equatorial Atmospheric Heat Transport: From the Seasonal Cycle to the Last Glacial Maximum. *Journal of Climate* **26**, 3597–3618 (2013).

29. S. M. Kang, Extratropical Influence on the Tropical Rainfall Distribution. *Current Climate Change Reports* **6**, 24–36 (2020).

30. R. Zhang, T. L. Delworth, Simulated Tropical Response to a Substantial Weakening of the Atlantic Thermohaline Circulation. *Journal of Climate* **18**, 1853–1860 (2005).

31. A. J. Broccoli, K. A. Dahl, R. J. Stouffer, Response of the ITCZ to Northern Hemisphere cooling. *Geophysical Research Letters* **33**, (2006).

32. D. M. W. Frierson, Y.-T. Hwang, Extratropical Influence on ITCZ Shifts in Slab Ocean Simulations of Global Warming. *Journal of Climate* **25**, 720–733 (2012).

33. J. Marshall, A. Donohoe, D. Ferreira, D. McGee, The ocean's role in setting the mean position of the Inter-Tropical Convergence Zone. *Clim Dyn* **42**, 1967–1979 (2014).

34. N. Sandeep, South Asian monsoon response to weakening of Atlantic meridional overturning circulation in a warming climate. *Climate Dynamics* **54**, 3507–3524 (2020).

35. E. Moreno-Chamarro, J. Marshall, T. L. Delworth, Linking ITCZ Migrations to the AMOC and North Atlantic/Pacific SST Decadal Variability. *Journal of Climate* **33**, 893–905 (2020).

36. X. Liu, N. Herold, M. Huber, Atlantic Meridional Overturning Circulation Influence on the Annual Mean Intertropical Convergence Zone Location in the Miocene. *Geophysical Research Letters* **51**, (2024).

37. C.-Y. Wang *et al.*, The influence of increasing temperatures on highland barley yields and on the maximum cultivation altitude on the Tibetan Plateau. *Advances in Climate Change Research* **14**, 573–579 (2023).

38. W. Cheng, J. C. H. Chiang, D. Zhang, Atlantic Meridional Overturning Circulation (AMOC) in CMIP5 Models: RCP and Historical Simulations. *Journal of Climate* **26**, 7187–7197 (2013).

39. S. Rahmstorf *et al.*, Exceptional twentieth-century slowdown in Atlantic Ocean overturning circulation. *Nature Clim Change* **5**, 475–480 (2015).

40. J. Zhu, Z. Liu, J. Zhang, W. Liu, AMOC response to global warming: dependence on the background climate and response timescale. *Clim Dyn* **44**, 3449–3468 (2015).

41. P. Nobre *et al.*, AMOC decline and recovery in a warmer climate. *Sci. Rep.* **13**, 15928 (2023).

42. Q. Zhang *et al.*, Simulating the mid-Holocene, last interglacial and mid-Pliocene climate with EC-Earth3-LR. *Geosci. Model Dev.* **14**, 1147–1169 (2021).

43. R. Döscher *et al.*, The EC-Earth3 Earth system model for the Coupled Model Intercomparison Project 6. *Geosci. Model Dev.* **15**, 2973–3020 (2022).

44. G. Balsamo et al., A revised hydrology for the ECMWF model: Verification from field site to terrestrial water storage and impact in the Integrated Forecast System. *J. Hydrometeorol.* **10**, 623–643 (2009).

45. G. Madec, "NEMO ocean engine", Note du Pole de modélisation, Institut Pierre-Simon Laplace (IPSL), France, No 27 ISSN No 1288-1619 (2008).

46. M. Vancoppenolle *et al.*, The Louvain-la-Neuve sea ice model, Notes du pole de modélisation, Institut Pierre-Simon Laplace (IPSL), Paris, France, No 31, ISSN No 1288-1619 (2012).

47. AL. Berger, Long-Term Variations of Daily Insolation and Quaternary Climatic Changes. *J. Atmos. Sci.* **35**, 2362–2367 (1978).

48. P. Köhler, C. Nehrbass-Ahles, J. Schmitt, T. F. Stocker, H. A. Fischer, 156 kyr smoothed history of the atmospheric greenhouse gases CO2, CH4, and N2O and their radiative forcing. *Earth Syst. Sci. Data* **9**, 363–387 (2017).

49. B. L. Otto-Bliesner *et al.*, The PMIP4 contribution to CMIP6 – Part 2: Two interglacials, scientific objective and experimental design for Holocene and Last Interglacial simulations, *Geosci. Model Dev.* **10**, 3979–4003 (2017).

50. R. C. Wills, T. Schneider, J. M. Wallace, D. S. Battisti, D. L. Hartmann, Disentangling Global Warming, Multidecadal Variability, and El Niño in Pacific Temperatures. *Geophysical Research Letters* **45**, 2487–2496 (2018).

Acknowledgments: This research is jointly supported by the Natural Science Foundation of China and by the foundation at the Shanghai Frontiers Science Centre of Atmosphere-Ocean Interaction of Fudan University. Q. Zhang acknowledges supports from Swedish Research Council, and the Swedish Foundation for International Cooperation in Research and Higher Education. The EC-Earth3-LR simulations were performed using ECMWF's computing and archive facilities and the Swedish National Infrastructure for Computing (SNIC) at the National Supercomputer Centre (NSC), which is partially funded by the Swedish Research Council.

Funding:

Natural Science Foundation of China grant 42230403 (PI, HY)

Natural Science Foundation of China grant 42288101

Swedish Foundation for International Cooperation in Research and Higher Education (STINT) grant MG2022-9298 (PI, QZ)

Swedish Research Council grant 2022-03129 (PI, QZ)

Author contributions:

Conceptualization: HY

Methodology: FA, HY, QZ

Investigation: FA, HY

Visualization: FA

Funding acquisition: HY, QZ

Supervision: HY, QZ

Writing – original draft: FA, HY

Writing – review & editing: HY, QZ

Model data: QZ, ZW

Proxy data: JH, HL, LH

Competing interests: Authors declare that they have no competing interests.

Data and materials availability: All data, code, and materials used in the analysis available upon request.

Supplementary Materials

Materials and Methods

Supplementary Text

figs. S1 to S5

References (*42–50*)

Science
AAAS

Supplementary Materials for

Multicentennial AMOC Variability Shaped the Hydroclimatic Stage for the Tubo Empire

Fengli An, Haijun Yang*, Qiong Zhang, Zhenqian Wang, Likun Han, Juzhi Hou, Hao Li

*Corresponding author. Haijun Yang, Email: yanghj@fudan.edu.cn

The PDF file includes:

Materials and Methods

Supplementary Text

figs. S1 to S5

References (*42-50*)

Materials and Methods

Model, Experiment and Methods

An 8000-year transient simulation spanning from 8000 BP to 1950 CE (Tr8K) produced by the EC-Earth3 (*42*) is analyzed in this study. This experiment follows the continuous evolution of Holocene climate and employs the EC-Earth3-Veg-LR configuration of the fully coupled Earth system model developed by the EC-Earth consortium (*42, 43*). The atmospheric component is the Integrated Forecasting System (IFS) of the European Centre for Medium-Range Weather Forecasts, coupled to the land surface model HTESSEL (*44*), both run at a horizontal resolution of TL159 (~1.125°). The ocean is simulated using NEMO3.6 (*45*), together with the LIM3 sea-ice model (*46*), at 1° horizontal resolution. All components are coupled through the OASIS3-MCT coupler (*43*). External forcings include time-varying orbital parameters computed internally in IFS following Berger (*47*), and annually varying greenhouse gas concentrations (CO_2, CH_4, N_2O) derived from ice-core reconstructions (*48*). The solar constant is prescribed at 1360.747 W m^{-2}. Aerosol fields, including dust and volcanic aerosols, are fixed at pre-industrial levels in line with the PMIP4 protocols (*49*).

The simulation is initialized from a pre-industrial control run, but with orbital parameters and greenhouse gas levels adjusted to 8 ka BP conditions. This setup was first integrated for ~300 years to allow the model to reach equilibrium, followed by another 700 years under constant forcings to ensure climate stability. The transient experiment was then started from this quasi-equilibrium state and integrated forward for 8000 years, with orbital and greenhouse gas forcings evolving continuously.

For this analysis, we focus on the last 2000 years of Tr8K to investigate the hydroclimatic context of the Tubo Empire. To focus on internally generated variability, we removed long-term orbital-scale trends from all variables. Given that most of the TP's precipitation occurs during boreal summer (June to September), our analyses primarily focus on these months unless otherwise noted. Summer averaged data includes precipitation, atmospheric wind and moisture flux, geopotential height, surface air temperature (SAT) and sea surface temperature (SST). For the Atlantic meridional overturning circulation (AMOC), annual mean data is used.

To isolate multicentennial variability from the model output, we apply Low-Frequency Component Analysis (LFCA) (*50*). LFCA extends traditional Empirical Orthogonal Function (EOF) analysis by emphasizing low-frequency variance, which avoids splitting one physical process into different modes and thus generating incorrect phase information when conducting correlation analysis. Based on traditional EOF analysis, the LFC1 is defined as linear combination of principal components with the largest proportion of low-frequency variance. Correspondingly, LFP1 is defined as the spatial pattern belonging to the LFC1. This method prioritizes physical processes operating at long timescales, providing a clearer representation of persistent internal variability. In this study, LFCA is used to extract the dominant low-frequency components of the AMOC and their associated hydroclimatic signatures over the TP. This

approach enables a robust assessment of how internal oceanic variability may have influenced regional climate and, potentially, the evolution of the Tubo Empire.

Throughout the following analysis, area-averaged fields are computed over 50°E–120°E, 5°–55°N, which encompasses but extends beyond the Tubo domain (Fig. 1). The raw AMOC index is defined as the maximum meridional overturning streamfunction between 200–3000 m at 20°–70°N. The Indian summer monsoon rainfall (ISMR) index is defined as the area-averaged June–September (JJAS) precipitation over 65°E–90°E and 10° N–30° N. The index for Intertropical convergence zone (ITCZ) is defined as the latitude value, within 65°E–90°E and 30°S–30°N, using the centroid approach (*32, 33*). That is, the latitude at which the cumulative JJAS rainfall to the north equals that to the south. The time series of ISMR and ITCZ plotted in our figures represent anomalies relative to their long-term seasonal climatology. A Butterworth low-pass filter with an 80-year cutoff period was applied to all time-series data wherever filtering is shown in the figures.

Finally, during 600–900 CE of the Tubo Empire, we partition the AMOC LFC1 record into two phases: strong AMOC, when the anomaly exceeds +1 standard deviation (σ), and weak AMOC, when it falls below –1 σ. These phase assignments are used in the composite analyses. Unless otherwise specified, all statistical analyses are limited to the time range from 600 to 900 CE to better represent the period of Tubo Empire.

Paleoclimate proxy data

To benchmark the modelled hydroclimate variability, we incorporate two published paleoclimate records from the southern TP (marked in Fig. 1). (1) Angrenjin Co – a millennial-length, pollen-based precipitation reconstruction (*17*) and (2) Jiang Co – a multi-proxy hydroclimate series derived from sedimentological and geochemical indicators (*18*). Both series are re-plotted alongside the EC-Earth3 output to provide proxy data context for regional precipitation changes during the Tubo period. Full analytical details are given in the original publications.

Historical records

To contextualize the simulated climate variability during the Tubo period, we refer to published historical reconstructions of climatic and societal conditions across the greater China region. In particular, we draw on documentary-based datasets compiled by Ge et al. (*23*), which synthesize climate-related events—such as droughts, floods, and temperature anomalies—based on official histories, local chronicles, and other historical documents. These reconstructions include multiple subregions, including parts of the TP, and provide valuable insights into regional hydroclimatic variability over the past two millennia. In this study, we use these records qualitatively to compare the timing of major climatic anomalies with the phases of the Tubo Empire's rise and decline.

Supplementary Text

Multicentennial variability in proxy records and coupled models' simulations

Robust multicentennial variability is identified in the Tr8K simulation (*19*), A detailed examination on 120 proxy records and transient Holocene simulations from 9 models discloses the significant multicentennial variability, with the dominant oscillation periods around 120-130 years and an average of 240 years. There is a comparatively good agreement between model and proxy data. All model simulations suggest that the Northern hemisphere high latitudes are the critical regions for the multicentennial variability, and the multicentennial variability is likely internally generated (*19*). The results indicate that internal mechanisms operate on multicentennial timescales, and the North Atlantic-Arctic is a region of interest for this aspect.

The multicentennial AMOC mode with a ~ 200-year period is also identified in a pre-industrial (PI) control simulation using the EC-Earth3-LR version (*20*). This mode is classified as an internal mode and originates predominately from the North Atlantic Ocean. The interplay between salinity advection feedback and vertical mixing in the subpolar North Atlantic plays key roles in providing the continues internal energy source to maintain the multicentennial oscillation. The perturbation flow of mean subtropical-subpolar salinity gradients serves as positive feedback to sustain the AMOC anomaly, while the mean advection of salinity anomalies and the vertical mixing or convection acts as negative feedback, constraining the AMOC anomaly. Notably, this low-frequency variability persists even in a warmer climate with doubled CO2 and weakened AMOC (*20*), emphasizing the robustness of the salinity advection feedback mechanism.

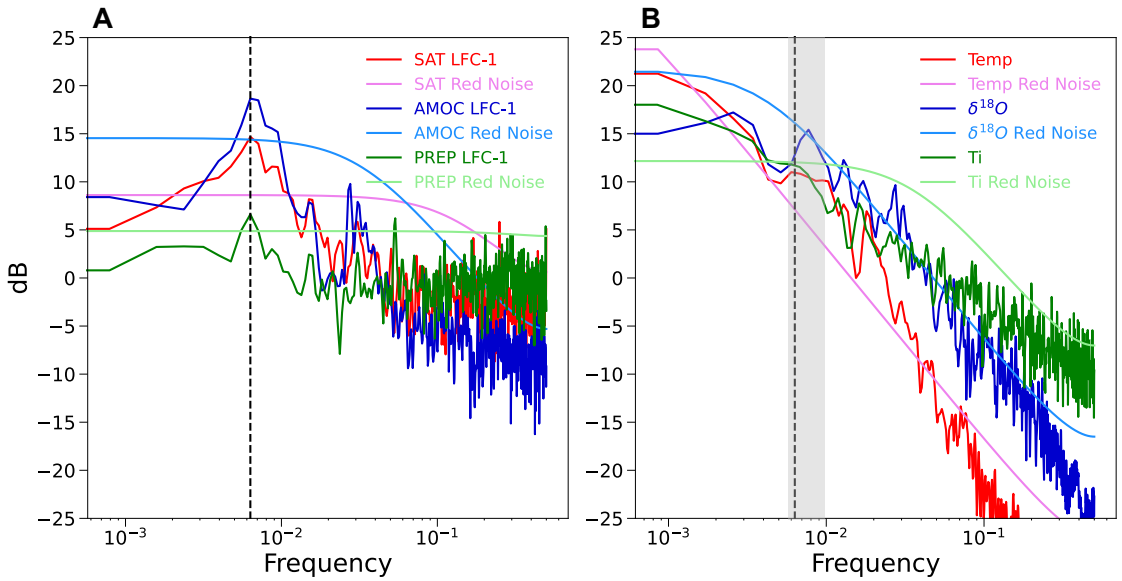

fig. S1. Power spectra of low-frequency model indices and proxy series. (**A**) Power spectrum charts(dB) of the unfiltered LFC1 index of summer precipitation (green) and SAT (red) over the Tubo region, and the AMOC LFC1 index (blue). Thin light-green, magenta, cyan curves give the respective first-order Markov (red-noise) backgrounds. The vertical dashed line marks the dominant peak at ~160 yr. (**B**) Same as (**A**) but for proxy series from Jiang Co: alkenone-based temperature (red), $\delta^{18}O$ (blue), and for Ti counts (green). Shaded grey band highlights the 100–180 yr window corresponding to the model-output peak in (**A**).

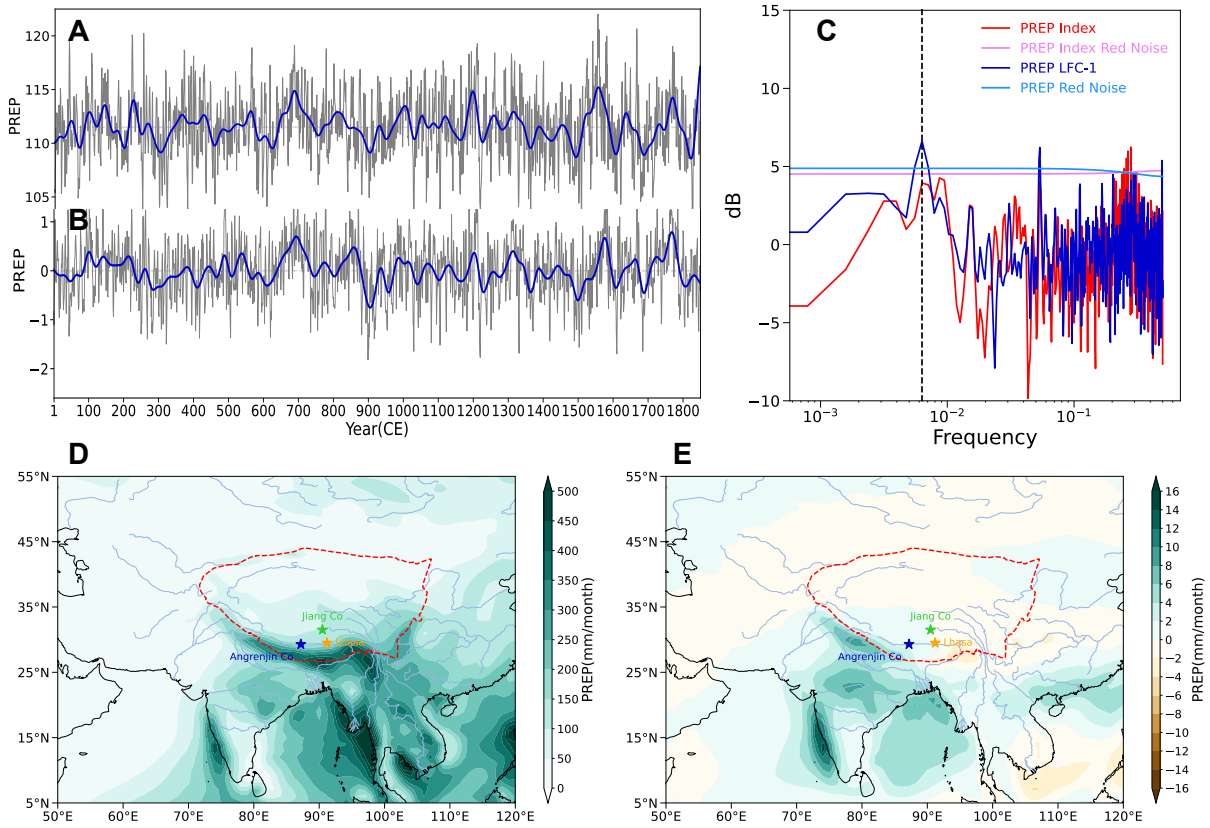

fig. S2. Comparison of basin-mean precipitation with its LFC1. (**A**) Raw summer precipitation index (mm month^{-1}) average over the South-Asian monsoon domain (5°N-55°N and 50°E-120°E) and period of 600-900 CE. (**B**) Normalized LFC1 time series of the same precipitation field. Thick blue curves in (**A**, **B**) are low-pass-filtered. (**C**) Power spectra (dB) of the raw regional-mean summer precipitation index (red) and its LFC1 (blue), with their corresponding first-order Markov red-noise backgrounds (magenta and light blue, respectively). The vertical dashed line highlights the ~160-yr peak shared by both series. (**D**) Climatological summer precipitation over the South-Asian monsoon domain (mm month^{-1}). (**E**) LFC1 pattern of summer precipitation (mm month^{-1}). Together, panels (**A**–**C**) confirm that the 160-yr oscillation dominates both the raw regional index and its LFC1, while panels (**D, E**) show that the LFC1 amplitude accounts for 5–10% of the climatological mean.

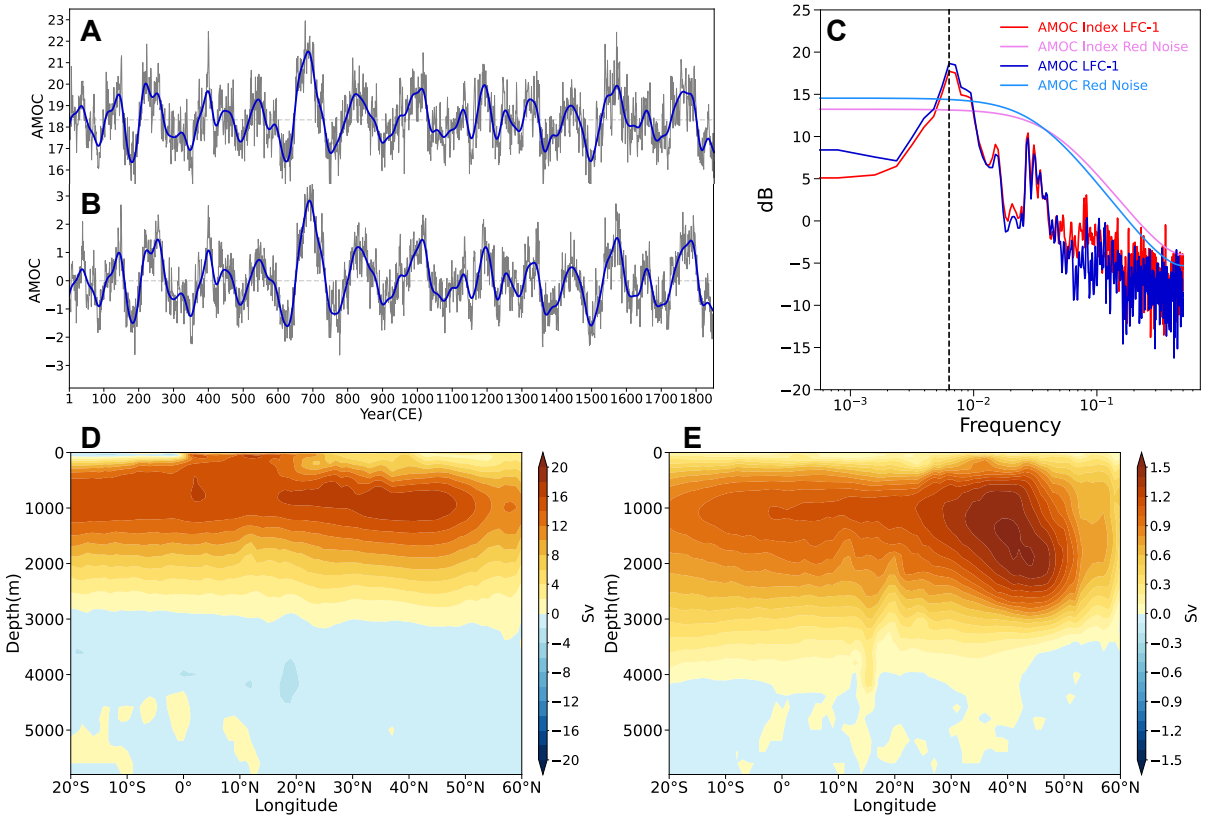

fig. S3. Comparison of climatological AMOC with its LFC1. (**A**) Raw AMOC index (Sv, 1 Sv=10^6 m^3 s^{-1}), defined as the annual-mean maximum overturning strength in the North Atlantic at 20°–70°N, 200–3000 m depth. (**B**) Normalized LFC1 index of the same AMOC. Thick blue curves in (**A**, **B**) are low-pass-filtered. (**C**) Power spectra (dB) of the raw AMOC index (red) and its LFC1 (blue) compared with their first-order Markov red-noise backgrounds (magenta and light-blue). Both series share a dominant peak ~160 yr (vertical dashed line). (**D**) Climatological AMOC pattern (Sv). (**E**) Spatial pattern of the AMOC LFC1 (LFP1). The LFC1 anomalies amplify the climatological cell in the North Atlantic, confirming that the LFC1 mode represents an amplitude fluctuation rather than a structural change. The LFC1 amplitude accounts for 10% of the climatological mean.

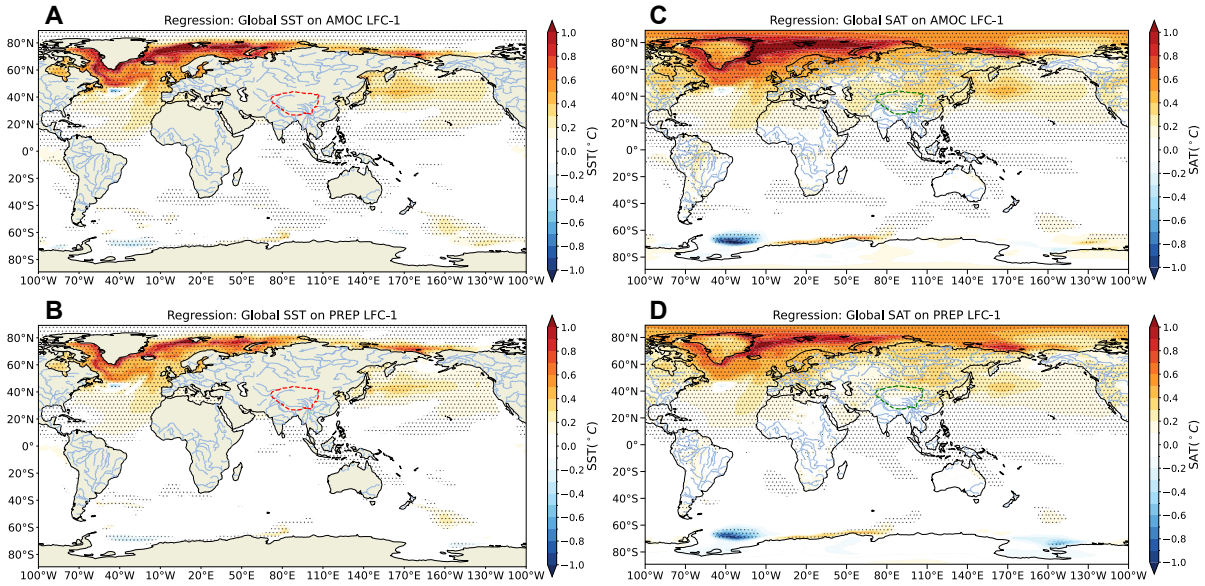

fig. S4. Regression of SST and SAT onto the LFC1 of AMOC and TP precipitation. (**A**, **B**) Regression of SST (°C) onto the LFC1 indexes of the AMOC the TP precipitation, respectively. (**C**, **D**) Same as (**A**, **B**), but for SAT regressions. Stippling denotes 99% significance (two-tailed t-test). Panels (**A**) and (**B**) reveal an almost identical basin-wide North Atlantic SST pattern; panels (**C**) and (**D**) show a matching SAT response. The congruent patterns confirm that North Atlantic SST anomalies act as the intermediary linking multicentennial AMOC variability to hydroclimatic changes over the Tibetan Plateau.

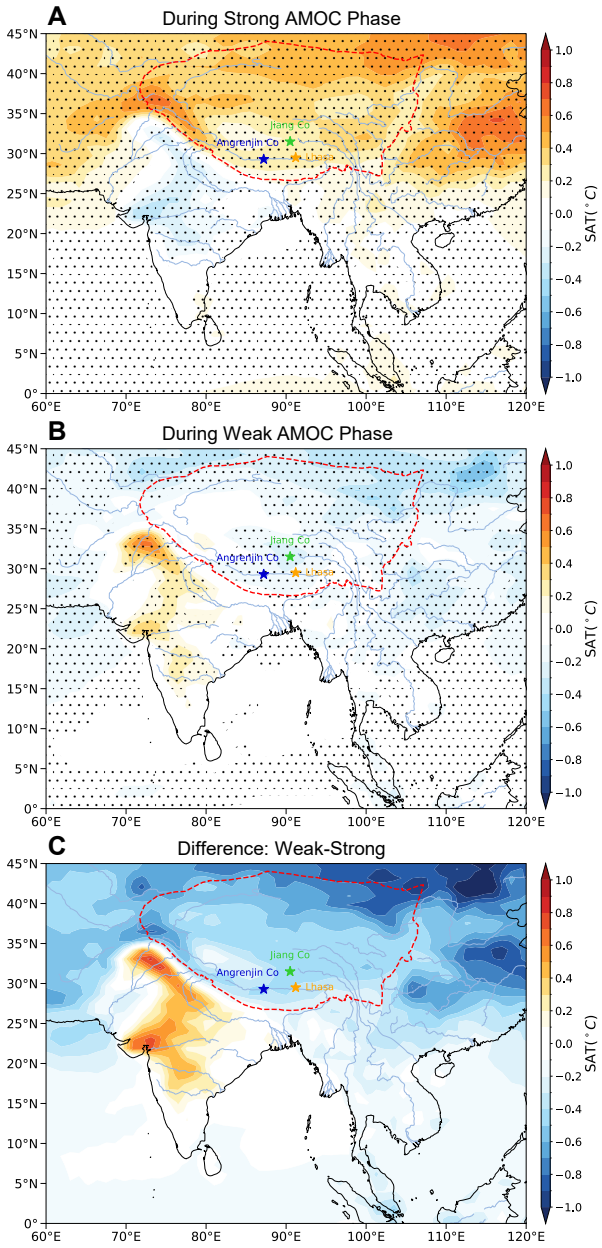

fig. S5. Composite summer SAT response to contrasting AMOC states. (**A**) Strong AMOC phases. (**B**) Weak AMOC phases. (**C**) Difference (weak – strong). SAT anomalies (°C) is shown with climatological SAT during 600-900 CE removed. Stippling in (**A**, **B**) marks 99% significance level.